A Helical Microwave Antenna for Welding Plaque During Balloon Angioplasty

Ping Liu and Carey M. Rappaport

Abstract—**A catheter-based microwave helix antenna has been developed in an attempt to improve the long-term success of balloon angioplasty treatment of arteriosclerosis. When the balloon is inflated to widen vessels obstructed with plaque, microwave power is deposited in the plaque, heating it, and thereby fixing it in place. By optimizing the helix pitch angle and excitation frequency, the antenna radiation pattern can be adjusted to deposit microwave power preferentially in the plaque while avoiding overheating the healthy artery. The optimal power deposition patterns of helical antennas are analytically computed for four-layered concentric and four-layered nonconcentric cylindrical geometries, which model symmetric and asymmetric occluded arteries. Experiments were performed on occluded artery phantom models with a prototype antenna for both symmetric and asymmetric models, which matched the theoretical predictions well, indicating almost complete power absorption in the low-water-content simulated plaque.**

I. Introduction

BALLOON angioplasty (or percutaneous transluminal coronary angioplasty) is becoming one of the most commonly performed major cardiac operations in the United States [1] and [2]. Compared to other cardiac surgical procedures, balloon angioplasty avoids cardiac bypass surgery, or other more traumatic operations, and has been very successful at both extending and improving the quality of life. Unfortunately, abrupt reclosure occurs in 3–5% of the cases in which balloon angioplasty is used [3], [4], and gradual restenosis of the artery occurs in 17–34% of the cases [5] and [6]. Fiber optic guided laser light has been used to irradiate and thermally fuse fragmented plaque pieces following coronary angioplasty [7] and [8]. However, when using laser energy, it is difficult to determine the proper laser intensity and length of exposure. Insufficient exposure results in poor welding, while too much injures the sensitive coronary artery.

An alternative physical process which can quickly deposit power in conductive media is microwave irradiation. Microwave and radio frequency (RF) energy has been used extensively in diathermy and hyperthermia cancer therapy [9] and [10] to noninvasively generate heat within tissue volumes. Although there are wide variations in the types of biological tissue, their electrical characteristics are usually grouped into two classes: high-water-content tissue (HWC), including muscle, organ, blood, and blood vessel walls; and low-water-content tissue (LWC), including fat and bone. The dielectric constants and conductivities of these two classes of tissue vary directly, though nonlinearly, with frequency, with values for HWC tissue being about one order of magnitude greater than those values for LWC tissue.

With such large differences in electrical characteristics between LWC and HWC tissue, radiation can be strongly reflected at tissue boundaries, and power dissipation will be greatly dependent on the angle of the incident wave. The governing equation [11] and [12] for the normal electric field at the boundary between the dielectrics is continuity of the normal component of electric flux density $\hat{\mathbf{n}} \cdot (\epsilon_1 \mathbf{E}_1 - \epsilon_2 \mathbf{E}_2) = 0$, where ϵ is the dielectric constant, and with unit normal $\hat{\mathbf{n}}$ pointing from LWC (1) to HWC (2) tissue. While the tangential electric field component is the same on both sides of the boundary: $\hat{\mathbf{n}} \times (\mathbf{E}_1 - \mathbf{E}_2) = 0$, the normal component is much smaller on the HWC side. Dissipated power P is given by $P = (\sigma/2)|\mathbf{E}|^2$, and since the conductivity is about one order of magnitude greater in HWC than LWC, the power deposited by a normally-polarized electric field on the HWC side can be much less than in the LWC (plaque) side. On the other hand, since tangentially polarized electric field is continuous across the boundary, approximately one order of magnitude more power would be deposited on the HWC (artery) side for this alternate polarization. Making use of the favorable normal electric field polarization, waves with a radially-polarized electric field will deposit more power in the plaque layer than in the healthy artery wall.

Microwave-assisted balloon angioplasty devices have been previously reported [13]–[17], but they tend either to generate electric field primarily tangentially to the artery wall, which may selectively overheat healthy tissue, or do not consider a more sophisticated multi-tissue artery. In this paper, an idealized four-layered concentric cylindrical geometry is first used to model the occluded artery. A more realistic four-layered nonconcentric geometry is then developed to model a real occluded artery. Finally, the results from the analytical computation are verified by an experimental model.

II. Concentric Four-Layered Cylindrical Model

It is important to select antenna sources which generate electric fields which will be most nearly radially oriented at the cylindrical interface between plaque and muscle. A reasonable choice is a helix designed to radiate a rapidly oscillating radially-polarized field [18] and [24]. Fig. 1 shows the relative positions of this helical antenna as part of an angioplasty balloon in the blood vessel.

Manuscript received September 28, 1995; revised March 11, 1996. This work supported by NIH Grant #R03 RR05333-01.

The authors are with the Electrical and Computer Engineering Department, Northeastern University, Boston, MA 02115 USA.

Publisher Item Identifier S 0018-9480(96)07028-7.

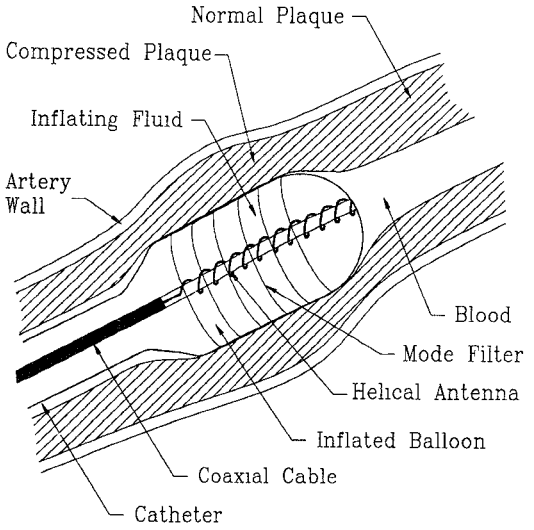

Fig 1 Helical antenna inside the balloon catheter.

A. Modal Analysis

Fig. 2(a) shows a four coaxially-layered geometry which models an idealized partially occluded artery. The innermost layer, region 1, is a teflon rod supporting the helical antenna with the helix at radius a_1. The second layer, region 2, is the opening enlarged by the balloon to radius a_2 through which blood will flow, filled during heating with a low-conductivity inflating fluid. This annular region is surrounded by the plaque layer, region 3, extending to radius a_3, which in turn is surrounded by healthy artery, region 4. The fourth region assumed to be infinitely thick, so that there are no appreciable reflections once the wave leaves the plaque layer. Although coronary artery walls are only about 2 mm thick, since the arteries are adjacent to the heart tissue and the serous fluid contained in the pericardium (both of which have the electromagnetic characteristics of HWC tissue) this outermost region can be modeled as an uniform high water content medium, several centimeters thick. Since the power radiated into HWC tissue at the frequencies of interest decays about two order of magnitude per centimeter, there will be no significant effects from structures outside the artery.

The source is analytically modeled as a sheath helix, with radius equal to a_1, positioned at the inner balloon layer, and with a surface current equal to $\mathbf{J}(z)$. Although the mathematical complexity of the following analysis is somewhat intimidating it is a reasonable model, as experimentally verified in [15]. However, it is approximate and is intended primarily for designing the experimental prototype. The sheath helix analysis [20] is used, and since there are many turns per axial wavelength, the electric and magnetic fields in each region are

$$E_{zq} = [U^q_{En} K_n(jk_{\rho q}\rho) + V^q_{En} I_n(jk_{\rho q}\rho)]\mathcal{P}(\phi, z) \quad (1)$$

$$E_{\rho q} = \frac{k_z}{k_{\rho q}} [U^q_{En} K_n'(jk_{\rho q}\rho) + V^q_{En} I_n'(jk_{\rho q}\rho)] \cdot \mathcal{P}(\phi, z) - \frac{n\omega\mu}{k^2_{\rho q}\rho} H_{zq} \quad (2)$$

$$E_{\phi q} = \frac{-nk_z}{k^2_{\rho q}\rho} E_{zq} - \frac{\omega\mu}{k_{\rho q}} [U^q_{Hn} K_n'(jk_{\rho q}\rho) + V^q_{Hn} I_n'(jk_{\rho q}\rho)]\mathcal{P}(\phi, z) \quad (3)$$

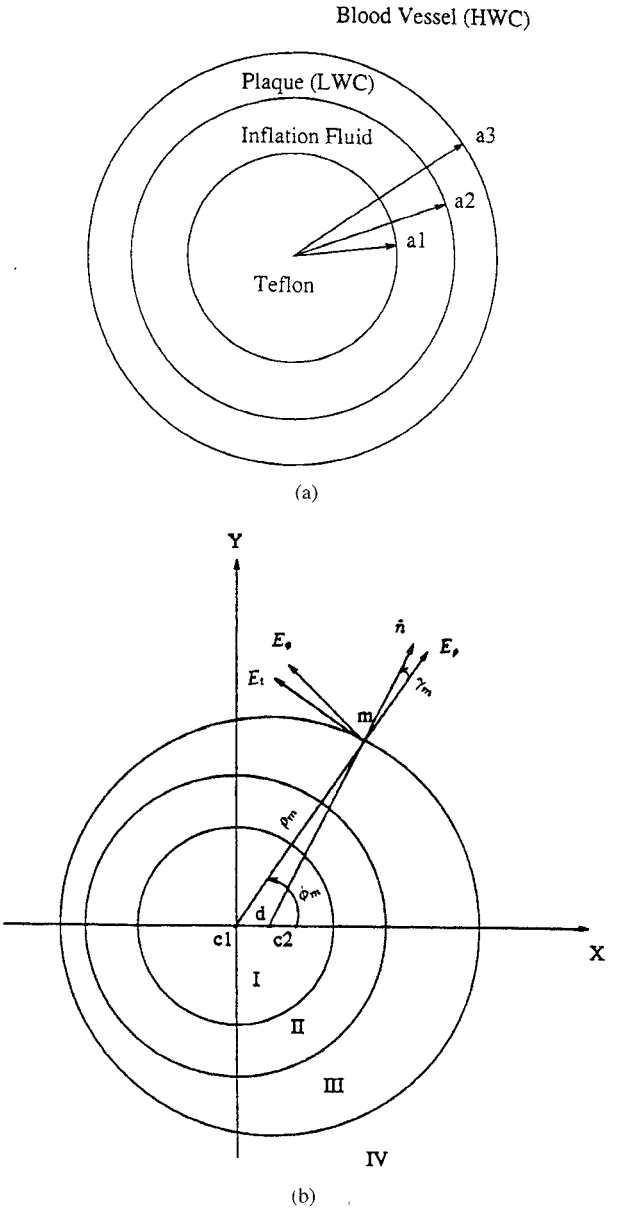

Fig 2. Cross section through a partially occluded artery. (a) Concentric geometry and (b) nonconcentric geometry

$$H_{zq} = [U^q_{Hn} K_n(jk_{\rho q}\rho) + V^q_{Hn} I_n(jk_{\rho q}\rho)]\mathcal{P}(\phi, z) \quad (4)$$

$$H_{\rho q} = \frac{n\omega\epsilon_q}{k^2_{\rho q}\rho} E_{zq} + \frac{k_z}{k_{\rho q}} [U^q_{Hn} K_n'(jk_{\rho q}\rho) + V^q_{Hn} I_n'(jk_{\rho q}\rho)]\mathcal{P}(\phi, z) \quad (5)$$

$$H_{\phi q} = \frac{\omega\epsilon_q}{k_{\rho q}} [U^q_{En} K_n'(jk_{\rho q}\rho) + V^q_{En} I_n'(jk_{\rho q}\rho)] \cdot \mathcal{P}(\phi, z) - \frac{nk_z}{k^2_{\rho q}\rho} H_{zq} \quad (6)$$

where $\mathcal{P}(\phi, z) = e^{jn\phi} e^{-jk_z z}$ is a common factor describing the field dependence on axial and circumferential variables, $q = 1, 2, 3, 4$ indicating region 1 (inside the helix), region 2 (between helix and inner plaque surface), region 3 (within the annular plaque layer), and region 4 (within the healthy artery). The variables $U^1_{En} = U^1_{Hn} = 0$, $V^1_{En} = A^1_n$, $V^1_{Hn} = B^1_n$, $U^2_{En} = A^2_n$, $U^2_{Hn} = B^2_n$, $V^2_{En} = C_n$, $V^2_{Hn} = D_n$, $U^3_{En} = A^3_n$,

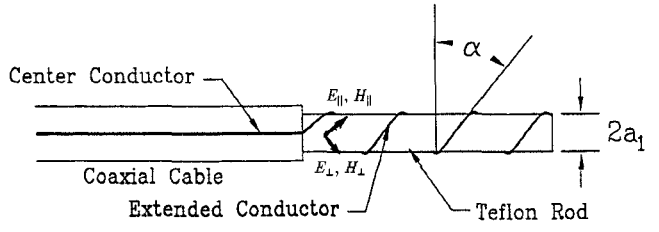

Fig. 3. The configuration of helical antenna.

$U^3_{Hn} = B^3_n$, $V^3_{En} = E_n$, $V^3_{Hn} = F_n$, $U^4_{En} = A^4_n$, $U^4_{Hn} = B^4_n$, $V^4_{En} = V^4_{Hn} = 0$; A^1_n, A^2_n, A^3_n, A^4_n, C_n, E_n, B^1_n, B^2_n, B^3_n, B^4_n, D_n, and F_n are unknown amplitude constants.

The sheath helix model does not consider launching or termination of waves. The coupling from coax cable to helix and the reflections from the end of the helix are not modeled, but rather optimized experimentally. The sheath helix model provides guidance in the choice of pitch angle α and feasibility of the concept.

To satisfy the boundary conditions for this four-layered cylindrical structure, the electric field on the cylindrical helical source surface must be oriented perpendicular to the wires. The magnetic field parallel to the wires is discontinuous across the cylinder source surface by an amount equal to the electric current density. Referring to Fig. 3, these boundary conditions are given by $E_{\|1} = E_{\|2} = 0$ and $H_{\|1} = H_{\|2}$. At the remaining boundaries, the tangential electric and magnetic fields are both continuous.

It is important to generate electric fields which will be most nearly radially-oriented at the cylindrical interface between plaque and muscle. A mode filter at the balloon/plaque interface can be used to eliminate the potentially dominant tangential E_ϕ component. The mode filter is modeled as multiple parallel, infinitesimally thin wires, bent around the vertical or z-axis until they rejoin themselves. Since these conducting wires are tangential to the cylindrical surface enclosing the helix antenna, they will force the circumferential electric field component to zero. Thus only the E_ρ and E_z components will be nonzero outside the mode filter. The mode filter can be fabricated by printing circumferential metal traces on the expanded balloon catheter.

Applying boundary conditions in (1)–(6) at $\rho = a_1$, for continuous E_z yields

$$I_n(jk_{\rho1}a_1)A^1_n - K_n(jk_{\rho2}a_1)A^2_n - I_n(jk_{\rho2}a_1)C_n = 0 \quad (7)$$

for continuous E_ϕ yields

$$\frac{jk_zn}{a_1}\left(\frac{1}{k^2_{\rho2}} - \frac{1}{k^2_{\rho1}}\right) I_n(jk_{\rho1}a_1)A^1_n - \frac{\omega\mu}{k_{\rho1}} I'_n(jk_{\rho1}a_1)B^1_n + \frac{\omega\mu}{k_{\rho2}} K'_n(jk_{\rho2}a_1)B^2_n + \frac{\omega\mu}{k_{\rho2}} I'_n(jk_{\rho2}a_1)D_n = 0 \quad (8)$$

for the continuous tangential magnetic field parallel to the helix $[(H_{z2} - H_{z1})\tan\alpha + H_{\phi2} - H_{\phi1} = 0]$

$$\frac{\omega\epsilon_1}{k_{\rho1}} I'_n(jk_{\rho1}a_1)A^1_n - \frac{\omega\epsilon_2}{k_{\rho2}} K'_n(jk_{\rho2}a_1)A^2_n - \frac{\omega\epsilon_2}{k_{\rho2}} I'_n(jk_{\rho2}a_1)C_n + I_n(jk_{\rho1}a_1)\left[\tan\alpha - \frac{jk_zn}{k^2_{\rho1}a_1}\right]B^1_n - K_n(jk_{\rho2}a_1)\left[\tan\alpha - \frac{jk_zn}{k^2_{\rho2}a_1}\right]B^2_n - I_n(jk_{\rho2}a_1)\left[\tan\alpha - \frac{jk_zn}{k^2_{\rho2}a_1}\right]D_n = 0 \quad (9)$$

and for the zero tangential electric field parallel to the sheath helix ($E_{z1}\tan\alpha + E_{\phi1} = 0$)

$$I_n(jk_{\rho1}a_1)\left[\tan\alpha - \frac{jk_zn}{k^2_{\rho1}a_1}\right]A^1_n - \frac{\omega\mu}{k_{\rho1}} I'_n(jk_{\rho1}a_1)B^1_n = 0. \quad (10)$$

At $\rho = a_2$, the boundary conditions for continuous E_z are

$$K_n(jk_{\rho2}a_2)A^2_n - I_n(jk_{\rho2}a_2)C_n - K_n(jk_{\rho3}a_2)A^3_n - I_n(jk_{\rho3}a_2)E_n = 0 \quad (11)$$

for the mode filter boundary conditions $E_{\phi2} = 0$

$$\frac{jk_zn}{k^2_{\rho2}a_2}[K_n(jk_{\rho2}a_2)A^2_n + I_n(jk_{\rho2}a_2)C_n] - \frac{\omega\mu}{k_{\rho2}}[K'_n(jk_{\rho2}a_2)B^2_n + I'_n(jk_{\rho2}a_2)D_n] = 0 \quad (12)$$

and $E_{\phi3} = 0$

$$\frac{jk_zn}{k^2_{\rho3}a_2}[K_n(jk_{\rho3}a_2)A^3_n + I_n(jk_{\rho3}a_2)E_n] - \frac{\omega\mu}{k_{\rho3}}[K'_n(jk_{\rho3}a_2)B^3_n + I'_n(jk_{\rho3}a_2)F_n] = 0 \quad (13)$$

and for continuous H_ϕ

$$\frac{\omega\epsilon_2}{k_{\rho2}} K'_n(jk_{\rho2}a_2)A^2_n + \frac{\omega\epsilon_2}{k_{\rho2}} I'_n(jk_{\rho2}a_2)C_n - \frac{\omega\epsilon_3}{k_{\rho3}} K'_n(jk_{\rho3}a_2)A^3_n - \frac{\omega\epsilon_3}{k_{\rho3}} I'_n(jk_{\rho3}a_2)E_n + \frac{jk_zn}{a_2}\cdot\left(\frac{1}{k^2_{\rho3}} - \frac{1}{k^2_{\rho2}}\right)[K_n(jk_{\rho2}a_2)B^2_n + I_n(jk_{\rho2}a_2)D_n] = 0. \quad (14)$$

At the last boundary $\rho = a_3$, the conditions are: for continuous E_z

$$K_n(jk_{\rho3}a_3)A^3_n - I_n(jk_{\rho3}a_3)E_n - K_n(jk_{\rho4}a_3)A^4_n = 0 \quad (15)$$

while for continuous E_ϕ

$$\frac{jk_zn}{a_3}\left(\frac{1}{k^2_{\rho3}} - \frac{1}{k^2_{\rho4}}\right)[K_n(jk_{\rho3}a_3)A^3_n + I_n(jk_{\rho3}a_3)E_n] - \frac{\omega\mu}{k_{\rho3}} K'_n(jk_{\rho3}a_3)B^3_n - \frac{\omega\mu}{k_{\rho3}} I'_n(jk_{\rho3}a_3)F_n + \frac{\omega\mu}{k_{\rho4}} K'_n(jk_{\rho4}a_3)B^4_n = 0 \quad (16)$$

for continuous H_z:

$$K_n(jk_{\rho3}a_3)B^3_n - I_n(jk_{\rho3}a_3)F_n - K_n(jk_{\rho4}a_3)B^4_n = 0. \quad (17)$$

Finally, for continuous H_ϕ

$$\frac{\omega\epsilon_3}{k_{\rho 3}} K_n'(jk_{\rho 3}a_3)A_n^3 + \frac{\omega\epsilon_3}{k_{\rho 3}} I_n'(jk_{\rho 3}a_3)E_n - \frac{\omega\epsilon_4}{k_{\rho 4}} K_n'(jk_{\rho 4}a_3)A_n^4 + \frac{jk_z n}{a_3}\left(\frac{1}{k_{\rho 4}^2} - \frac{1}{k_{\rho 3}^2}\right) \cdot [K_n(jk_{\rho 3}a_3)B_n^3 + I_n(jk_{\rho 3}a_3)F_n] = 0. \quad (18)$$

Because not all the constants A_n^1, A_n^2, C_n, A_n^3, E_n, A_n^4, B_n^1, B_n^2, D_n, B_n^3, F_n, and B_n^4 are equal to zero, the determinant of the matrix which multiplies these constant coefficients of the above equations (the eigenvalue function) must be equal to zero, giving the eigenvalue equation.

The electric characteristic of the material supporting the helix is very similar to the inflating fluid (such as nonconductive physiologically benign fluid, the perfluorocarbon Fluosol^{TM} [21]). Thus it is reasonable to assume that their dielectric constants and conductivities are equal, i.e., $\epsilon_1 = \epsilon_2$ and $\sigma_1 = \sigma_2$. This assumption simplifies the above eigenvalue equation. Additionally, because of the symmetry of the geometry, only the dominant mode, $n = 0$, will be considered here. This assumption had been experimentally verified in a similar helical antenna structure [15]. Thus further simplification [22] reduces the eigenvalue equation to the following 4×4 matrix equation

$$\det(\overline{\overline{\mathbf{M}}}) = \begin{vmatrix} \mathcal{C}_{11} & \mathcal{C}_{12} & \mathcal{C}_{13} & \mathcal{C}_{14} \\ \mathcal{C}_{21} & \mathcal{C}_{22} & \mathcal{C}_{23} & \mathcal{C}_{24} \\ 0 & 0 & \mathcal{C}_{33} & \mathcal{C}_{34} \\ \mathcal{C}_{41} & \mathcal{C}_{42} & 0 & 0 \end{vmatrix} = 0 \quad (19)$$

where

$$\mathcal{C}_{11} = K_0(jk_{\rho 1}a_2)$$
$$\mathcal{C}_{12} = I_0(jk_{\rho 1}a_2)$$
$$\mathcal{C}_{13} = -K_0(jk_{\rho 3}a_2)$$
$$\mathcal{C}_{14} = -I_0(jI_{\rho 3}a_2)$$
$$\mathcal{C}_{21} = \frac{1}{\eta_1} K_0'(jk_{\rho 1}a_2)$$
$$\mathcal{C}_{22} = \frac{1}{\eta_1} I_0'(jk_{\rho 1}a_2)$$
$$\mathcal{C}_{23} = -\frac{1}{\eta_3} K_0'(jk_{\rho 3}a_2)$$
$$\mathcal{C}_{24} = -\frac{1}{\eta_3} I_0'(jk_{\rho 3}a_2)$$
$$\mathcal{C}_{33} = \frac{\omega\underline{\epsilon_3}}{k_{\rho 3}} K_0'(jk_{\rho 3}a_3)K_0(jk_{\rho 4}a_3) - \frac{\omega\underline{\epsilon_4}}{k_{\rho 4}} K_0(jk_{\rho 3}a_2)K_0'(jk_{\rho 4}a_3)$$
$$\mathcal{C}_{34} = \frac{\omega\underline{\epsilon_3}}{k_{\rho 3}} I_0'(jk_{\rho 3}a_3)K_0(jk_{\rho 4}a_3) - \frac{\omega\underline{\epsilon_4}}{k_{\rho 4}} I_0(jk_{\rho 3}a_2)K_0'(jk_{\rho 4}a_3)$$
$$\mathcal{C}_{41} = I_0(jk_{\rho 1}a_1)I_0'(jk_{\rho 1}a_2)K_0(jK_{\rho 1}a_1) - \frac{\omega^2\mu\underline{\epsilon_1}\cot^2\alpha}{k_{\rho 1}^2} I_0'(jk_{\rho 1}a_1) \cdot [I_0'(jk_{\rho 1}a_2)K_0'(jk_{\rho 1}a_1) - I_0'(jk_{\rho 1}a_1)K_0'(jk_{\rho 1}a_2)]$$
$$\mathcal{C}_{42} = I_0^2(jk_{\rho 1}a_1)I_0'(jk_{\rho 1}a_2).$$

Solving this eigenvalue equation gives the axial propagation constant k_z, which therefore leads to the electric field distribution throughout the entire structure.

B. Optimum Power Deposition Pattern

Using different values for the dielectric constants and conductivities of plaque and healthy artery at different frequencies, as well as different pitch angles, different values are obtained for the axial propagation constant k_z, which leads to the radial propagation constant in each region $k_{\rho\ 1,2,3,4}$. Once the propagation constants are known, the electric field distributions throughout the entire structure can be found by replacing any one of the 12 equations (7)–(18) with one giving the appropriate excitation.

Commercial balloon dilatation catheters are commonly available in sizes from 2 to 6 mm inflated radius [23]. For example, a 4 mm radius balloon with a 7 French catheter is identified as Boston Scientific part number BMX/8-3/7/75. Using helix radius $a_1 = 2.5$ mm, and typical dilated balloon radius $a_2 = 4$ mm and dilated artery radius $a_3 = 5$ mm, computer simulations of the power solutions at various frequencies and pitch angles have been performed. Smaller pitch angles have better performance with a greater percentage drop in power from plaque to healthy artery tissue. Fig. 4 shows the dissipated power as a function of radius for various pitch angles at the experimentally optimized frequency of 1.6 GHz. The pitch angle $\alpha = 17°$ provides a large drop in power across the interface for all frequencies from 100 MHz to 10 GHz as shown in Fig. 5. The power drops off rapidly at the artery wall, protecting it from overheating. This figure also shows that lower frequencies have better performance. Initially, since the eventual impedance characteristics of this helical antenna in lossy tissue were unknown, it was important to select a helix pitch angle with as much broadband performance as possible. Although Fig. 4 indicates that a 10° pitch angle would yield a greater power drop at the plaque/artery interface at 1.6 GHz, the 17° pitch angle is used since it affords more frequency flexibility, and thus may be less sensitive to small variations in geometry and tissue electromagnetic characteristics. The normal and tangential electric field components for a pitch angle of 17° at 1.6 GHz is shown in Fig. 6. Note that the ϕ and z components are continuous, while the ρ component is much larger on the plaque side of boundary. Clearly, the ϕ component is eliminated by the mode filter and the electric fields are almost entirely radially oriented at the cylindrical interface between plaque and artery at pitch angle $\alpha = 17°$.

Electric fields are almost radially oriented at the cylindrical interface between plaque and artery and the power clearly drops off rapidly in the artery wall if the appropriate helical antenna pitch angle is chosen. What happens if the balloon size (a_2) or artery size (a_3) is different? It is important to verify that the helical antenna source can work with different balloon and artery sizes. Figs. 7 and 8 show that at 8 GHz, the power still drops off rapidly at the artery wall

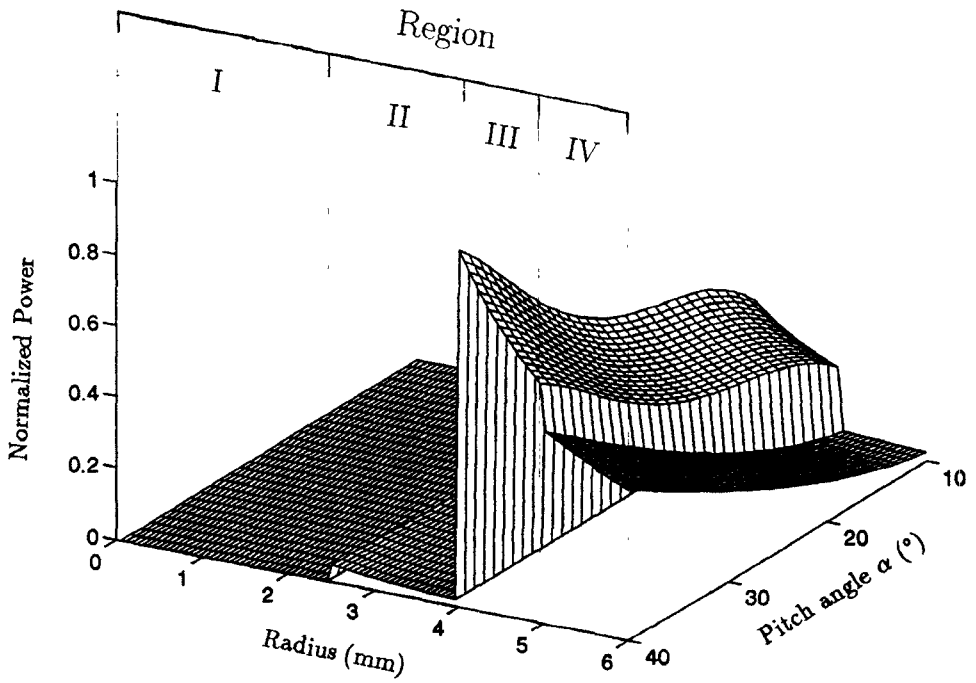

Fig. 4. Dissipated power distribution as a function of radius for various pitch angles at 1.6 GHz.

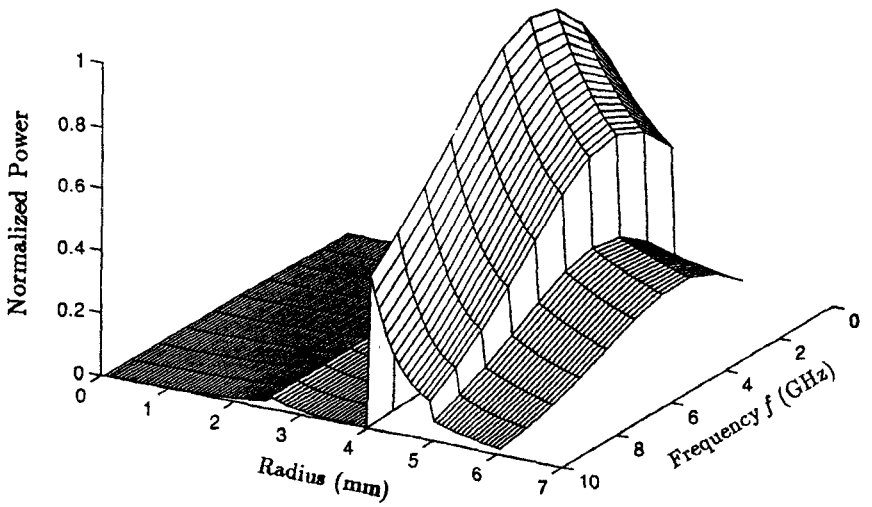

Fig. 5. Dissipated power distribution as a function of radius for various frequencies at a pitch angle of 17°.

for any choice of plaque thickness with constant outer or inner diameter, respectively. Similar results are found for most of the frequencies considered.

Thus, it is concluded that the appropriate antenna source can generate greater power in the plaque than in the artery at quite wide frequency range and flexible balloon and artery sizes.

III. Nonconcentric Four-Layered Cylindrical Model

It has been demonstrated that a power deposition pattern can be generated with more power deposited in the plaque than anywhere else, and that will heat the plaque without overheating healthy artery tissue, with an appropriate helical antenna as the source for an idealized concentric four-layered cylindrical geometry. Since plaque occlusions most often occur asymmetrically, it is essential to show that the electric field intensity and the deposited power are also concentrated in this LWC tissue layer even when it is predominantly on one side of the artery. Intuitively, it is reasonable to assume field distributions in off-center geometries will be similar to concentric geometries. In order to analytically rather than numerically build a mathematical model for calculating the electric field intensity and the power deposition, a four-layered nonconcentric circular cylindrical geometry is used [24]. This section presents this new model which is closer to real blockage as well as a new method for optimizing the power distribution of such a model.

A. Modal Analysis

Fig. 2(b) shows a nonconcentric geometry which models such a partially occluded artery. It consists of four layers:

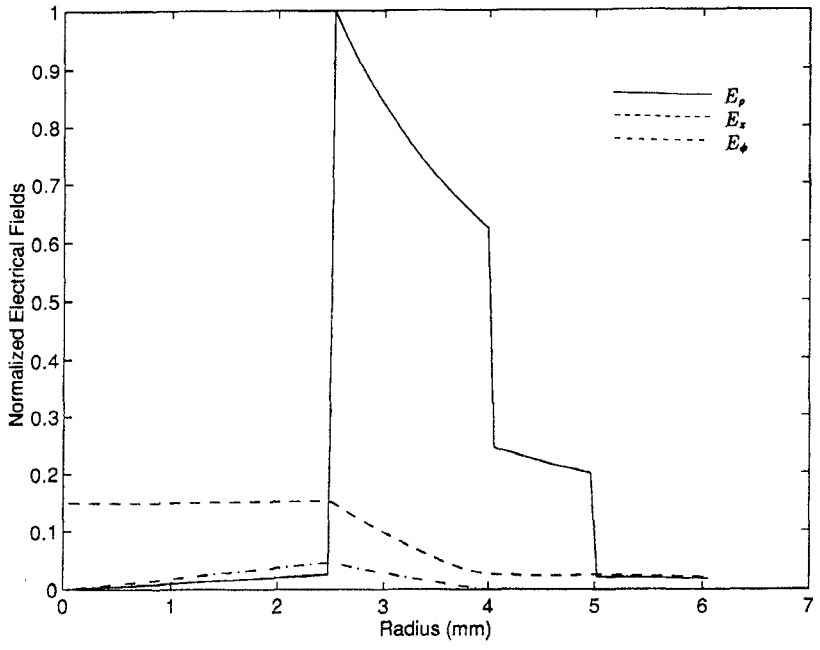

Fig. 6. Three electric field components for pitch angle $\alpha = 17°$ at 1.6 GHz.

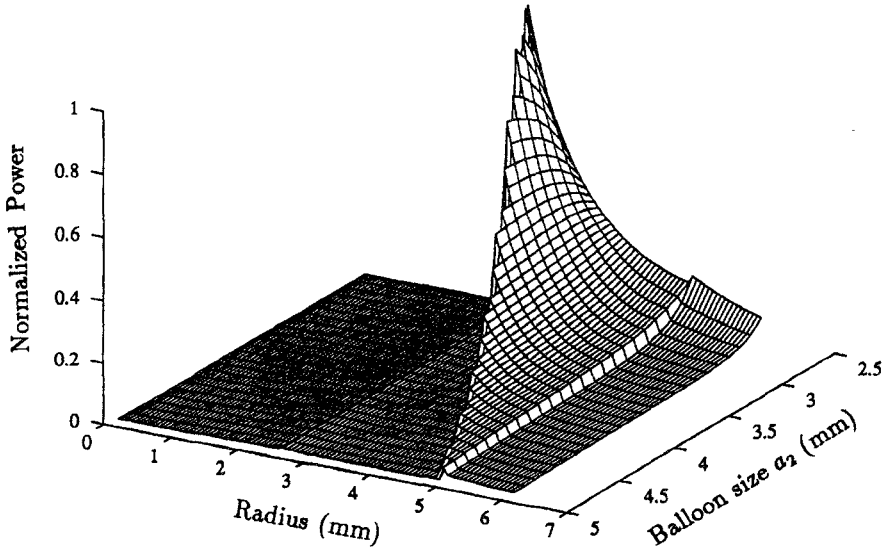

Fig. 7. Dissipated power distribution as a function of radius for various a_2 at a 17° pitch angle at 8 GHz.

the inner helix support, the inflation fluid layer (within the balloon), the plaque layer, and the external healthy blood vessel region, which is again assumed to extend to infinite radius. The helix and balloon boundaries are concentric, as before, but the circular plaque/artery interface has its center displaced a distance d from the axis of the balloon.

The source is analytically modeled as a tape helix, with radius equal to a_1, positioned at the inner balloon layer, and with a surface current equal to $\mathbf{J}(z)$, as before. The fields and boundary conditions are similar to those given in the concentric geometry except for the two outer nonconcentric regions and their boundaries. A mode filter is again used in this asymmetric model to eliminate the tangential field. By first considering the two boundary conditions at $\rho = a_1$ and $\rho = a_2$, eight equations are obtained with the ten unknown amplitude coefficients A_m^1, A_m^2, C_m, A_m^3, E_m, B_m^1, B_m^2, D_m, B_m^3, and F_m, where $m = 0, 1, \cdots, \infty$. [refer to (7)–(14)]. By solving these eight equations, A_m^1, A_m^2, C_m, A_m^3, B_m^1, B_m^2, D_m, and B_m^3 can be written in terms of E_m and F_m, for example

$$A_m^3 = \frac{\mathcal{U}_{em}}{\mathcal{R}_m} E_m + \frac{\mathcal{U}_{fm}}{\mathcal{R}_m} F_m \tag{20}$$

$$B_m^3 = \frac{\mathcal{V}_{em}}{\mathcal{R}_m} E_m + \frac{\mathcal{V}_{fm}}{\mathcal{R}_m} F_m \tag{21}$$

where $\mathcal{U}_{em}$, $\mathcal{U}_{fm}$, $\mathcal{V}_{em}$, $\mathcal{V}_{fm}$, and $\mathcal{R}_m$ are the determinants of the coefficient matrices and are only functions of frequency, pitch angle α, radii a_1, and a_2, complex tissue permittivities $\underline{\epsilon_1}$, $\underline{\epsilon_2}$, and $\underline{\epsilon_3}$, and the unknown axial wave number k_z.

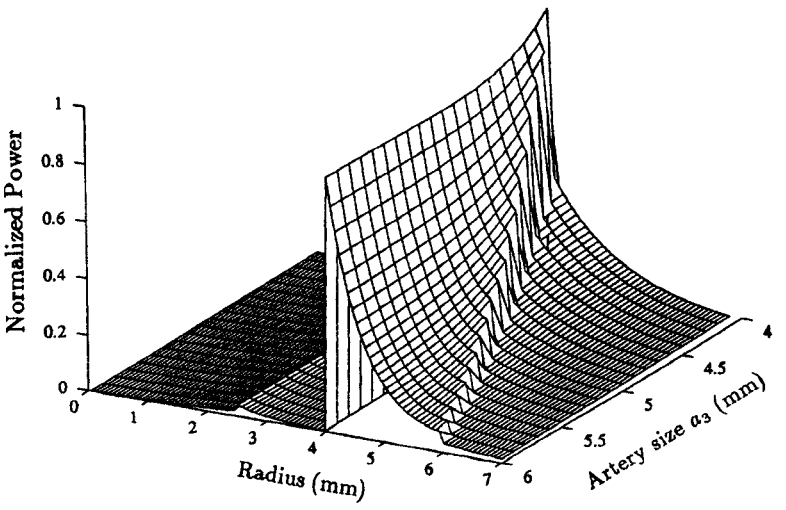

Fig. 8. Dissipated power distribution as a function of radius for various a_3 at a 17° pitch angle at 8 GHz.

The axial components of fields in the plaque layer can then be written as

$$E_{z3} = \sum_{n=0}^{\infty} [\mathcal{X}_{\mathcal{U}e}(\rho, n)E_n + \mathcal{X}_{\mathcal{U}f}(\rho, n)F_n]\mathcal{P}(\phi, z) \quad (22)$$

$$H_{z3} = \sum_{n=0}^{\infty} [\mathcal{X}_{\mathcal{V}e}(\rho, n)E_n + \mathcal{X}_{\mathcal{V}f}(\rho, n)F_n]\mathcal{P}(\phi, z) \quad (23)$$

where

$$\mathcal{X}_{\mathcal{U}e}(\rho, n) = (\mathcal{U}_{en}/\mathcal{R}_n)K_n(jk_{\rho 3}\rho) + I_n(jk_{\rho 3}\rho), \mathcal{X}_{\mathcal{U}f}(\rho, n) = (\mathcal{U}_{fn}/\mathcal{R}_n)K_n(jk_{\rho 3}\rho)\mathcal{X}_{\mathcal{V}e}(\rho, n) = (\mathcal{V}_{en}/\mathcal{R}_n)K_n(jk_{\rho 3}\rho),$$
$$\mathcal{X}_{\mathcal{V}f}(\rho, n) = (\mathcal{V}_{fn}/\mathcal{R}_n)K_n(jk_{\rho 3}\rho) + I_n(jk_{\rho 3}\rho).$$

At the remaining boundary between plaque layer and healthy artery, the boundary conditions require the tangential electric and magnetic fields to both be continuous, i.e.,

$$E_{z3}(\rho_m, \phi_m, z) = E_{z4}(\rho_m, \phi_m, z)$$
$$E_{t3}(\rho_m, \phi_m, z) = E_{t4}(\rho_m, \phi_m, z)$$
$$H_{z3}(\rho_m, \phi_m, z) = H_{z4}(\rho_m, \phi_m, z)$$
$$H_{t3}(\rho_m, \phi_m, z) = H_{t4}(\rho_m, \phi_m, z)$$

where $E_{ti} = E_{\phi i}\cos\gamma_m - E_{\rho i}\sin\gamma_m$ and $H_{ti} = H_{\phi i}\cos\gamma_m - H_{\rho i}\sin\gamma_m$ $(i = 3, 4)$. Here, γ_m is the angle between two nonconcentric radial lines at a point m on the boundary, ρ_m is the radial distance, and ϕ_m is the circumferential angle from x-axis, as shown in Fig. 2(b).

Substituting in electric and magnetic fields equations, we obtain

$$\sum_{n=0}^{\infty} [\mathcal{X}_{\mathcal{U}e}(\rho_m, n)E_n + \mathcal{X}_{\mathcal{U}f}(\rho_m, n)F_n - K_n(jk_{\rho 4}\rho_m)A_n^4]\mathcal{P}(\phi_m, z) = 0 \quad (24)$$

$$\sum_{n=0}^{\infty} [\mathcal{X}_{\mathcal{V}e}(\rho_m, n)E_n + \mathcal{X}_{\mathcal{V}f}(\rho_m, n)F_n - K_n(jk_{\rho 4}\rho_m)B_n^4]\mathcal{P}(\phi_m, z) = 0 \quad (25)$$

$$\sum_{n=0}^{\infty} \left(\left\{ \left[\frac{jk_z\sigma_n}{k_{\rho 3}^2\rho_m} \mathcal{X}_{\mathcal{U}e}(\rho_m, n) - \frac{\omega\mu}{k_{\rho 3}} \mathcal{X}'_{\mathcal{V}e}(\rho_m, n) \right] \cos\gamma_m - \left[\frac{k_z}{k_{\rho 3}} \mathcal{X}'_{\mathcal{U}e}(\rho_m, n) - \frac{j\omega\mu\sigma_n}{k_{\rho 3}^2\rho_m} \mathcal{X}_{\mathcal{V}e}(\rho_m, n) \right] \sin\gamma_m \right\} E_n + \left\{ \left[\frac{jk_z\sigma_n}{k_{\rho 3}^2\rho_m} \mathcal{X}_{\mathcal{U}f}(\rho_m, n) - \frac{\omega\mu}{k_{\rho 3}} \mathcal{X}'_{\mathcal{V}f}(\rho_m, n) \right] \cos\gamma_m - \left[\frac{k_z}{k_{\rho 3}} \mathcal{X}'_{\mathcal{U}f}(\rho_m, n) - \frac{j\omega\mu\sigma_n}{k_{\rho 3}^2\rho_m} \mathcal{X}_{\mathcal{V}f}(\rho_m, n) \right] \sin\gamma_m \right\} F_n - \mathcal{Y}_{mn}^- A_n^4 + \mathcal{Z}_{mn}^-(\mu)B_n^4 \right) = 0 \quad (26)$$

$$\sum_{n=0}^{\infty} \left(\left\{ \left[\frac{\omega\epsilon_3}{k_{\rho 3}} \mathcal{X}'_{\mathcal{U}e}(\rho_m, n) - \frac{jk_z\sigma_n}{k_{\rho 3}^2\rho_m} \mathcal{X}_{\mathcal{V}e}(\rho_m, n) \right] \cos\gamma_m + \left[\frac{j\omega\epsilon_3\sigma_n}{k_{\rho 3}^2\rho_m} \mathcal{X}_{\mathcal{U}e}(\rho_m, n) - \frac{k_z}{k_{\rho 3}} \mathcal{X}'_{\mathcal{V}e}(\rho_m, n) \right] \sin\gamma_m \right\} E_n + \left\{ \left[\frac{\omega\epsilon_3}{k_{\rho 3}} \mathcal{X}'_{\mathcal{U}f}(\rho_m, n) - \frac{jk_z\sigma_n}{k_{\rho 3}^2\rho_m} \mathcal{X}_{\mathcal{V}f}(\rho_m, n) \right] \cos\gamma_m + \left[\frac{j\omega\epsilon_3\sigma_n}{k_{\rho 3}^2\rho_m} \mathcal{X}_{\mathcal{U}f}(\rho_m, n) - \frac{k_z}{k_{\rho 3}} \mathcal{X}'_{\mathcal{V}f}(\rho_m, n) \right] \sin\gamma_m \right\} F_n - \mathcal{Z}_{mn}^+(\epsilon_4)A_n^4 + \mathcal{Y}_{mn}^+ B_n^4 \right) = 0 \quad (27)$$

where

$$\mathcal{X}'_{\mathcal{U}e}(\rho, n) = (\mathcal{U}_{en}/\mathcal{R}_n)K'_n(jk_{\rho 3}\rho) + I'_n(jk_{\rho 3}\rho), \quad \mathcal{X}'_{\mathcal{U}f}(\rho, n) = (\mathcal{U}_{fn}/\mathcal{R}_n)K'_n(jk_{\rho 3}\rho), \quad \mathcal{X}'_{\mathcal{V}e}(\rho, n) = (\mathcal{V}_{en}/\mathcal{R}_n)K'_n(jk_{\rho 3}\rho), \quad \mathcal{X}'_{\mathcal{V}f}(\rho, n) = (\mathcal{V}_{fn}/\mathcal{R}_n)K'_n(jk_{\rho 3}\rho) + I'_n(jk_{\rho 3}\rho),$$
$$\mathcal{Y}_{mn}^{\pm} = (jk_z\sigma_n/k_{\rho 4}^2\rho_m)K_n(jk_{\rho 4}\rho_m)\cos\gamma_m \pm (k_z/k_{\rho 4})K'_n(jk_{\rho 4}\rho_m)\sin\gamma_m,$$
$$\mathcal{Z}_{mn}^{\pm}(\mathcal{C}) = (\omega\mathcal{C}/k_{\rho 4})K'_n(jk_{\rho 4}\rho_m)\cos\gamma_m \pm (j\omega\mathcal{C}\sigma_n/k_{\rho 4}^2\rho_m)K_n(jk_{\rho 4}\rho_m)\sin\gamma_m,$$

and

$$\phi_m = \frac{\pi}{N-1}m, \quad m = 0, 1, \cdots, N-1 \quad (28)$$

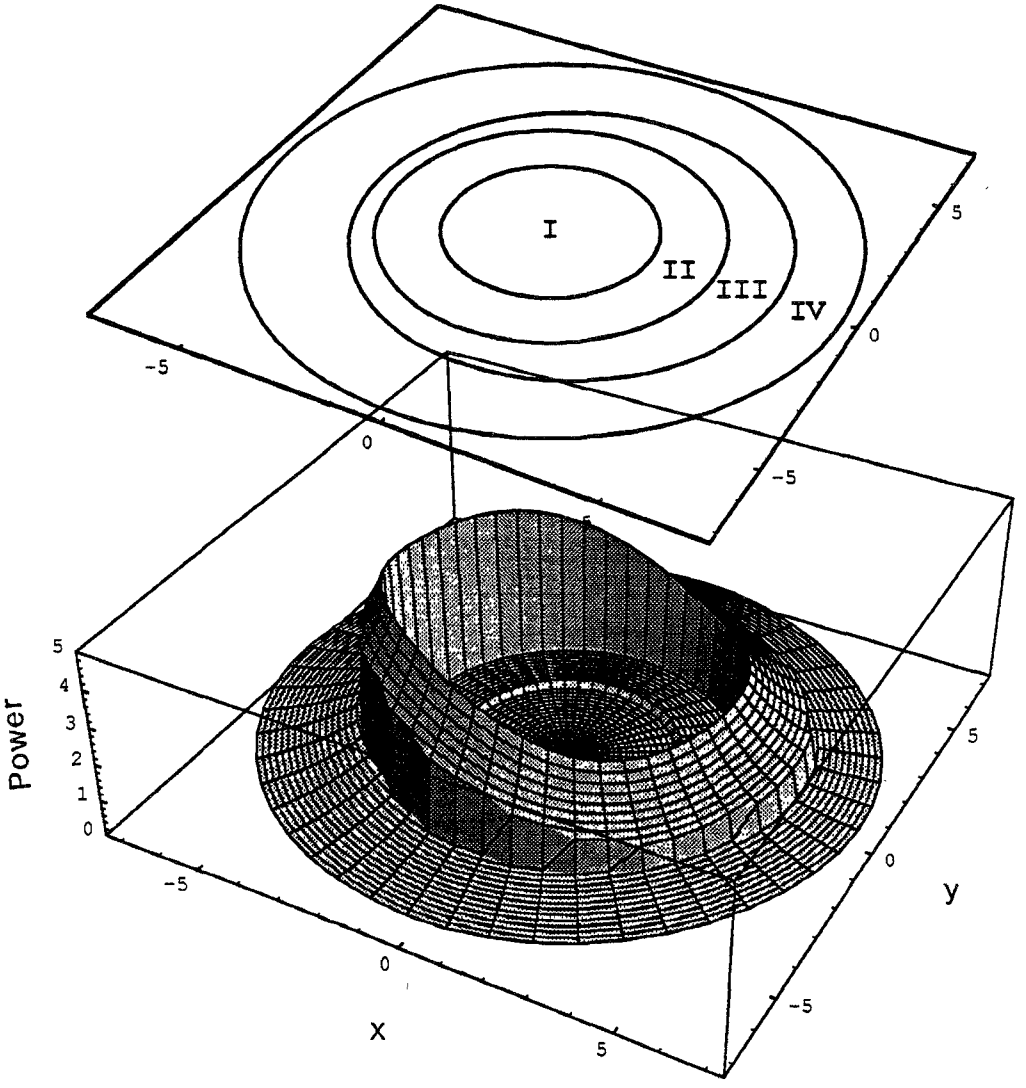

Fig. 9. Dissipated power distribution as a function of radius and circumferential angle at 1.5 GHz and offset 0.5 mm.

$$\sin \gamma_m = \frac{d}{a_3} \sin \phi_m \tag{29}$$

$$\rho_m = a_3(\cos \gamma_m + \cot \phi_m \sin \gamma_m). \tag{30}$$

Truncating the infinite series to N terms and matching the above four equations at N discrete points on the boundary results in a homogeneous system of $4N$ linear equations in the $4N$ unknowns: E_n, F_n, A_n^4, and B_n^4. The $4N \times 4N$ matrix $\overline{\overline{\mathbf{N}}}$ is derived in the Appendix. Because not all the unknown constants are equal to zero, the determinant of the matrix of the unknowns $\overline{\overline{\mathbf{N}}}$ must be zero. Using several determinant reduction steps, followed by a two-dimensional (2-D) search technique to solve the eigenvalue function, now gives the complex propagation constant k_z, which therefore gives the electric field distributions throughout the entire structure.

B. Optimum Power Deposition Pattern

Using helix radius $a_1 = 2.5$ mm, typical dilated balloon radius $a_2 = 4$ mm and artery radius $a_3 = 5$ mm, computer simulations of the power solutions at various frequencies and various off-center distances have been performed. Fig. 9 shows the dissipated power as a function of radius and circumferential angle at frequency 1.5 GHz, pitch angle 17° with an offset $d = 0.5$ mm. In this case, the plaque is three times thicker on one side of the artery model than the other. The power clearly drops off rapidly in the artery wall, protecting it from overheating the healthy artery tissue.

The normal and tangential electric field components at four typical circumferential sampling positions $\phi = 0°$, $\phi = 90°$, $\phi = 180°$, and $\phi = 270°$ are shown in Fig. 10 for the same antenna of Fig. 9. Note that the ϕ components at 90° and 270° are not continuous at the boundary between plaque and artery, because they are not tangential for off-center circle except at $\phi = 0°$ and $\phi = 180°$. The ρ component is much larger on the plaque side of boundary. Electric fields are almost radially oriented at the cylindrical interface between plaque and artery.

As in the concentric geometry mode, it is important to verify that the helical antenna source can work with different balloon sizes and artery sizes. Fig. 11 shows a power distribution with differing helix radii, balloon sizes and artery sizes. Clearly, greater power is deposited in the plaque, protecting healthy artery from overheating.

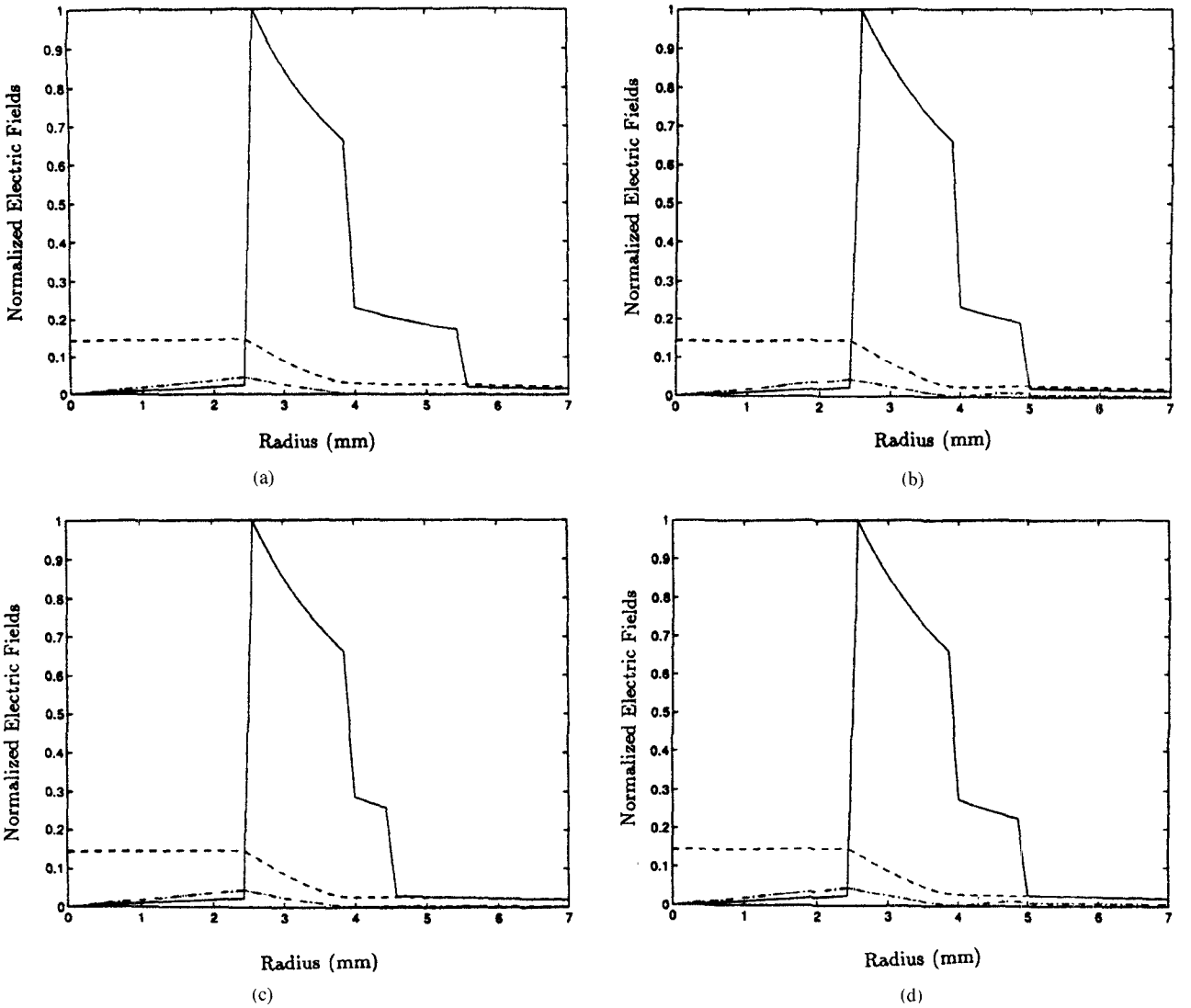

Fig. 10. Electric field components for $f = 1.5$ GHz, $d = 0$ 5 mm, and $\alpha = 17°$ at sampling position: (a) $\phi = 0°$, (b) $\phi = 90°$, (c) $\phi = 180°$, (d) $\phi = 270°$.

IV. Experimental System and Results

The experimental test system for measuring the power deposition from a helical angioplasty antenna consists of a helical antenna, an electric field probe, an alignment fixture, simulated plaque and artery phantom, and the HP8510 automated network analyzer system, as shown schematically in Fig. 12. Note that the mode filter, though present, is not explicitly shown.

The helical antenna is made of very fine insulated copper wire, connected to the center conductor of a semi-rigid coaxial cable, and also coiled around a circular teflon cylinder mounted on one end of the coaxial cable. The antenna radius is 2.5 mm, and its pitch angle is 17°. The other end of the coaxial cable is mated to the source port of the Network Analyzer. The field radiated by the test antenna is measured using a monopole probe, made from another coaxial cable, with one end having the 1 mm center conductor extend beyond the outer conductor and the other end connected to the load port of the HP8510. The plaque phantom is a hard circular cylindrical shell, mixed according to the fat/bone recipe by Guy [25] which surrounds the helical antenna. Several tiny evenly spaced holes were drilled along the plastic plaque phantom, so the probe could measure the radiated electric field within the phantom, which could then be used to compute deposited power. The fixture is a plastic box, calibrated for uniform field sampling position. It not only holds the helical and probe antennas, but contains the liquid sucrose/saline artery phantom [26].

The helical antenna and the electric field probe are modeled as a two-port network. According to two-port network theory, S_{11} gives the ratio of power reflected back from the antenna under test, and hence gives a measure of how well the helical antenna radiates power into phantom media, while S_{21} represents how well the power is transferred between the two antennas through the phantom. Experiments show that the reflected signal $|S_{11}|$ is minimized near 1.64 GHz with a value of -33.5 dB for the four-layered concentric model and near 1.59 GHz with a value of -35.5 dB for the four-layered nonconcentric model. Values of $|S_{21}|$ are measured for various radius positions along the coaxial line. The holes not used for a given measurement are covered by tape to exclude the artery phantom liquid. For measurements outside the plaque

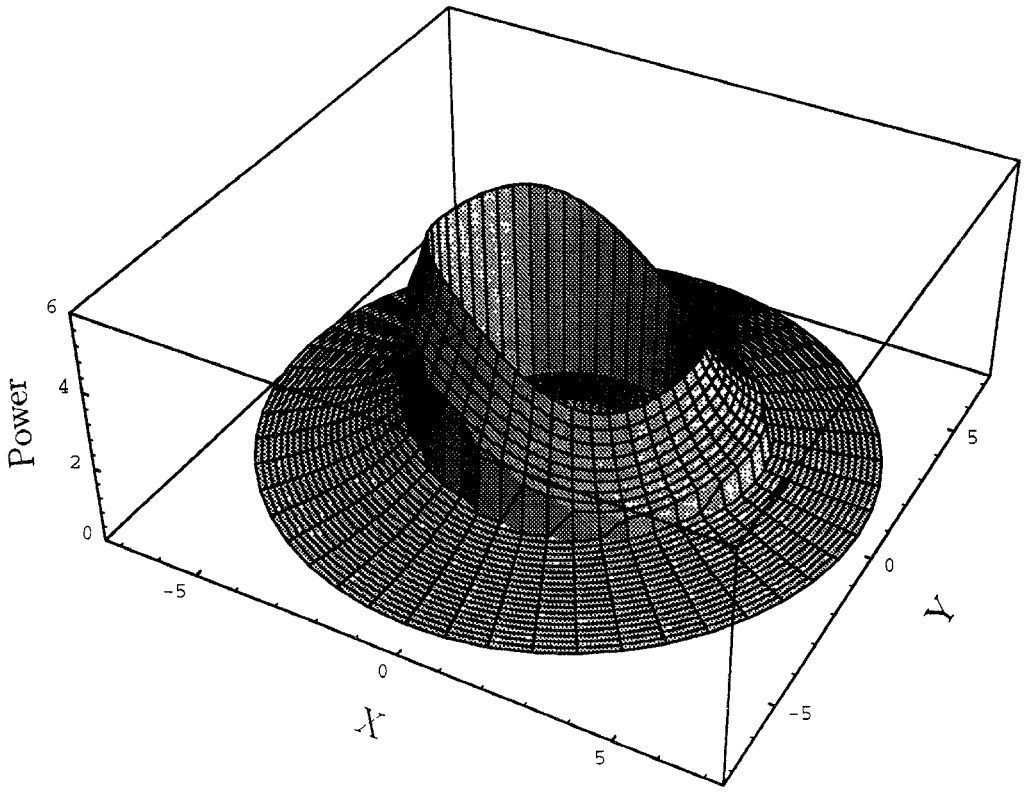

Fig. 11. Dissipated power distribution as a function of radius and circumferential angle with helix radius 1.5 mm, balloon size 3 mm, artery size 4 mm, and offset 0.5 mm.

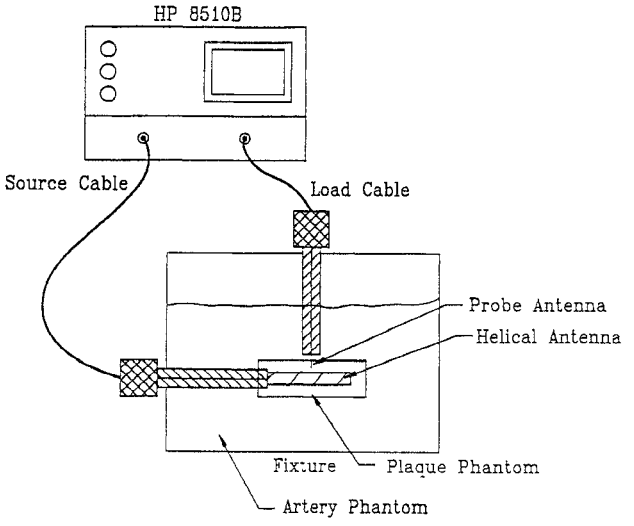

Fig 12. Schematic diagram of the experiment to measure the radiated electric field distribution of the helical antenna.

phantom (in the artery phantom), the field is much less intense than within the plaque, and it decays very rapidly with radius. As such, accurate measurements with the finite length probe antenna are problematic, and large error bars must be used to display field values. Experiments also confirm that tangential electric field is much smaller than the normal electric field.

Many measurements were performed with the helical antenna/probe combination, and the results were consistent and repeatable. Fig. 13 is a plot of the measured results and theoretical calculations as a function of radius for the concentric four-layered model. Fig. 14 shows three typical values (plaque field at balloon/plaque boundary, plaque field at plaque/artery boundary, and artery field at plaque/artery boundary) for experimental results and theoretical calculations as a function of circumferential angle for the nonconcentric four-layered model. These plots compare favorably with the theoretically calculated values.

It is clear that the maximum power deposition in the artery wall is less than the minimum power deposited in the plaque layer for both the four-layered concentric and the four-layered nonconcentric models. The experimental results agreed well with the computer simulations. The simulated four-layered nonconcentric behavior is a good model for real artery. It is shown that preferential plaque heating by microwave radiation is feasible.

V. Summary

A helical microwave antenna heating device has been developed for use in conjunction with balloon angioplasty to weld human plaque/arterial wall separations and alleviate reclosure and restenosis. This antenna applicator will be small enough to be inserted within a dilation catheter, with microwave power supplied by a thin coaxial transmission line. The fields radiated by the helix are optimized by adjusting the wave frequency and helix pitch, to establish power deposition patterns which preferentially heat plaque while sparing healthy artery wall tissue.

An idealized concentric four-layered cylindrical geometry was used to model the occluded artery. The field and power

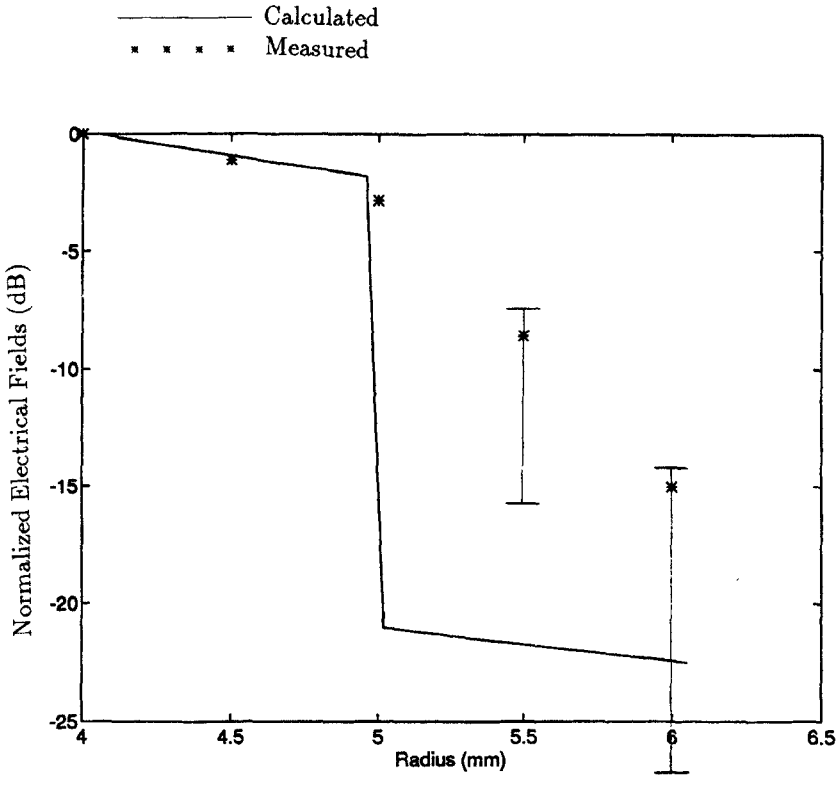

Fig. 13. Calculated and measured radial electric fields as a function of radius.

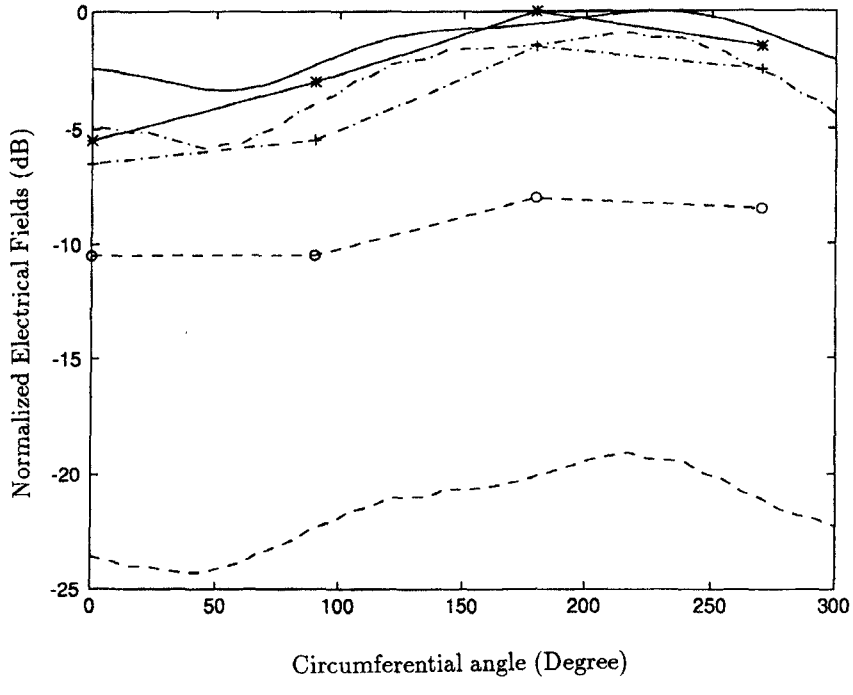

Fig. 14. Calculated and measured results as a function of circumferential angle.

distributions were optimized as a function of frequency and helix pitch angle. Broad-band optimization indicated that the best pitch angle was 17° for greatest plaque/artery discrimination. The power deposited by a helix with pitch angle 17° is greater in the plaque layer than in the artery wall for different balloon sizes and artery sizes across a wide frequency band.

A more realistic nonconcentric four-layered cylindrical geometry was developed to model the real occluded artery. The resulting analytic model based on solving boundary condition series equations is much more complicated than that of the symmetric case. Results indicate that even for a three to one plaque asymmetry, a helix with a 17° pitch angle generates

almost radially polarized electric fields and therefore deposits significantly more power in the plaque layer. Greater power is also deposited in the plaque for different balloon and artery sizes. The feasibility of using a helix with this more realistic nonconcentric model is thus demonstrated. The theoretical results show that power is preferentially deposited in the plaque layer for both the idealized concentric model and the more realistic nonconcentric model.

A helix antenna based on these design formulas was fabricated and experimentally tested. The power deposition within the plaque layer, plaque/artery wall interface, and within the artery wall was measured using an HP8510 network analyzer. The computational and experimental results are a proof-of-principle that preferential plaque heating by microwave radiation is feasible. Computer simulations clearly show minimal healthy artery illumination, and experiments agreed well with these simulations. It is hoped that this microwave antenna angioplasty balloon will be a valuable addition to coronary angioplasty.

APPENDIX

The $4N \times 4N$ matrix resulting from (24)–(27) is

$$\begin{bmatrix} [\mathcal{E}^1_{mn}] & [\mathcal{F}^1_{mn}] & [\mathcal{A}^1_{mn}] & [\mathcal{B}^1_{mn}] \\ [\mathcal{E}^2_{mn}] & [\mathcal{F}^2_{mn}] & [\mathcal{A}^2_{mn}] & [\mathcal{B}^2_{mn}] \\ [\mathcal{E}^3_{mn}] & [\mathcal{F}^3_{mn}] & [\mathcal{A}^3_{mn}] & [\mathcal{B}^3_{mn}] \\ [\mathcal{E}^4_{mn}] & [\mathcal{F}^4_{mn}] & [\mathcal{A}^4_{mn}] & [\mathcal{B}^4_{mn}] \end{bmatrix} \begin{bmatrix} [E_n] \\ [F_n] \\ [A^4_n] \\ [B^4_n] \end{bmatrix} = \overline{\mathbf{0}} \tag{A1}$$

where

$$[\mathcal{E}^i_{mn}] = \begin{bmatrix} e^i_{0,0} & e^i_{0,1} & \cdots & e^i_{0,N-1} \\ e^i_{1,0} & e^i_{1,1} & \cdots & e^i_{1,N-1} \\ \vdots & \vdots & \ddots & \vdots \\ e^i_{N-1,0} & e^i_{N-1,1} & \cdots & e^i_{N-1,N-1} \end{bmatrix}$$

$$[\mathcal{F}^i_{mn}] = \begin{bmatrix} f^i_{0,0} & f^i_{0,1} & \cdots & f^i_{0,N-1} \\ f^i_{1,0} & f^i_{1,1} & \cdots & f^i_{1,N-1} \\ \vdots & \vdots & \ddots & \vdots \\ f^i_{N-1,0} & f^i_{N-1,1} & \cdots & f^i_{N-1,N-1} \end{bmatrix}$$

$$[\mathcal{A}^i_{mn}] = \begin{bmatrix} a^i_{0,0} & a^i_{0,1} & \cdots & a^i_{0,N-1} \\ a^i_{1,0} & a^i_{1,1} & \cdots & a^i_{1,N-1} \\ \vdots & \vdots & \ddots & \vdots \\ a^i_{N-1,0} & a^i_{N-1,1} & \cdots & a^i_{N-1,N-1} \end{bmatrix}$$

$$[\mathcal{B}^i_{mn}] = \begin{bmatrix} b^i_{0,0} & b^i_{0,1} & \cdots & b^i_{0,N-1} \\ b^i_{1,0} & b^i_{1,1} & \cdots & b^i_{1,N-1} \\ \vdots & \vdots & \ddots & \vdots \\ b^i_{N-1,0} & b^i_{N-1,1} & \cdots & b^i_{N-1,N-1} \end{bmatrix}$$

$i = 1, 2, 3, 4$, being the first, the second, the third, and the fourth row block of (A1).

$$[E_n] = \begin{bmatrix} e_0 \\ e_1 \\ \vdots \\ e_{N-1} \end{bmatrix}$$

$$[F_n] = \begin{bmatrix} f_0 \\ f_1 \\ \vdots \\ f_{N-1} \end{bmatrix}$$

$$[A^4_n] = \begin{bmatrix} a_{40} \\ a_{41} \\ \vdots \\ a_{4N-1} \end{bmatrix}$$

$$[B^4_n] = \begin{bmatrix} b_{40} \\ b_{41} \\ \vdots \\ b_{4N-1} \end{bmatrix}$$

$$e^1_{m,n} = \mathcal{R}_n \mathcal{X}_{\mathcal{U}e}(\rho_m, n) \cos(n\phi_m) \tag{A2}$$

$$e^2_{m,n} = \mathcal{V}_{en} K_n(jk_{\rho 3}\rho_m) \sin(n\phi_m) \tag{A3}$$

$$e^3_{m,n} = \left[\frac{jk_z n}{k^2_{\rho 3}\rho_m}\mathcal{R}_n \mathcal{X}_{\mathcal{U}e}(\rho_m, n) - \frac{\omega\mu}{k_{\rho 3}}\mathcal{V}_{en}K'_n(jk_{\rho 3}\rho_m)\right] \cdot \cos\gamma_m \sin(n\phi_m) - \left[\frac{k_z}{k_{\rho 3}}\mathcal{R}_n \mathcal{X}'_{\mathcal{U}e}(\rho_m, n) + \frac{j\omega\mu n}{k^2_{\rho 3}\rho_m}\mathcal{V}_{en}K_n(jk_{\rho 3}\rho_m)\right] \cdot \sin\gamma_m \cos(n\phi_m) \tag{A4}$$

$$e^4_{m,n} = \left[\frac{\omega\epsilon_3}{k_{\rho 3}}\mathcal{R}_n \mathcal{X}'_{\mathcal{U}e}(\rho_m, n) + \frac{jk_z n}{k^2_{\rho 3}\rho_m}\mathcal{V}_{en}K_n(jk_{\rho 3}\rho_m)\right] \cdot \cos\gamma_m \cos(n\phi_m) + \left[\frac{j\omega\epsilon_3 n}{k^2_{\rho 3}\rho_m}\mathcal{R}_n \mathcal{X}_{\mathcal{U}e}(\rho_m, n) + \frac{k_z}{k_{\rho 3}}\mathcal{V}_{en}K'_n(jk_{\rho 3}\rho_m)\right] \cdot \sin\gamma_m \sin(n\phi_m) \tag{A5}$$

$$f^1_{m,n} = \mathcal{U}_{fn}K_n(jk_{\rho 3}\rho_m) \cos(n\phi_m) \tag{A6}$$

$$f^2_{m,n} = \mathcal{R}_n \mathcal{X}_{\mathcal{V}f}(\rho_m, n) \sin(n\phi_m) \tag{A7}$$

$$f^3_{m,n} = \left[\frac{jk_z n}{k^2_{\rho 3}\rho_m}\mathcal{U}_{fn}K_n(jk_{\rho 3}\rho_m) - \frac{\omega\mu}{k_{\rho 3}}\mathcal{R}_n \mathcal{X}'_{\mathcal{V}f}(\rho_m, n)\right] \cdot \cos\gamma_m \sin(n\phi_m) - \left[\frac{k_z}{k_{\rho 3}}\mathcal{U}_{fn}K'_n(jk_{\rho 3}\rho_m) + \frac{j\omega\mu n}{k^2_{\rho 3}\rho_m}\mathcal{R}_n \mathcal{X}_{\mathcal{V}f}(\rho_m, n)\right] \cdot \sin\gamma_m \cos(n\phi_m) \tag{A8}$$

$$f^4_{m,n} = \left[\frac{\omega\epsilon_3}{k_{\rho 3}}\mathcal{U}_{fn}K'_n(jk_{\rho 3}\rho_m) + \frac{jk_z n}{k^2_{\rho 3}\rho_m}\mathcal{R}_n \mathcal{X}_{\mathcal{V}f}(\rho_m, n)\right] \cdot \cos\gamma_m \cos(n\phi_m) + \left[\frac{j\omega\epsilon_3 n}{k^2_{\rho 3}\rho_m}\mathcal{U}_{fn}K_n(jk_{\rho 3}\rho_m) + \frac{k_z}{k_{\rho 3}}\mathcal{R}_n \mathcal{X}'_{\mathcal{V}f}(\rho_m, n)\right] \cdot \sin\gamma_m \sin(n\phi_m) \tag{A9}$$

$$a^1_{m,n} = -K_n(jk_{\rho 4}\rho_m)\cos(n\phi_m) \tag{A10}$$

$$a^2_{m,n} = 0 \tag{A11}$$

$$a^3_{m,n} = -\frac{jk_z n}{k^2_{\rho 4}\rho_m}K_n(jk_{\rho 4}\rho_m)\cos\gamma_m \sin(n\phi_m) + \frac{k_z}{k_{\rho 4}}K'_n(jk_{\rho 3}\rho_m)\sin\gamma_m\cos(n\phi_m) \tag{A12}$$

$$a^4_{m,n} = -\frac{\omega\epsilon_4}{k_{\rho 4}}K'_n(jk_{\rho 4}\rho_m)\cos\gamma_m\cos(n\phi_m) + \frac{j\omega\epsilon_4 n}{k^2_{\rho 4}\rho_m}\sin\gamma_m\sin(n\phi_m) \tag{A13}$$

$$b^1_{m,n} = 0 \tag{A14}$$

$$b^2_{m,n} = -K_n(jk_{\rho 4}\rho_m)\sin(n\phi_m) \tag{A15}$$

$$b^3_{m,n} = \frac{\omega\mu}{k_{\rho 4}}K'_n(jk_{\rho 4}\rho_m)\cos\gamma_m\sin(n\phi_m) + \frac{j\omega\mu n}{k^2_{\rho 4}\rho_m}K_n(jk_{\rho 4}\rho_m)\sin\gamma_m\cos(n\phi_m) \tag{A16}$$

$$b^4_{m,n} = \frac{jk_z n}{k^2_{\rho 4}\rho_m}K_n(jk_{\rho 4}\rho_m)\cos\gamma_m\cos(n\phi_m) + \frac{k_z}{k_{\rho 4}}K'_n(jk_{\rho 4}\rho_m)\sin\gamma_m\sin(n\phi_m) \tag{A17}$$

Equation (A1) must be solved numerically using (for example) a 2-D linear search technique.

ACKNOWLEDGMENT

Authors gratefully acknowledge helpful discussion with A. Morgenthaler, L. Zhang, and Z. Jin and appreciate helpful suggestions of three anonymous reviewers.

REFERENCES

[1] K. M. Kent *et al.*, "Long-term efficacy of percutaneous transluminal coronary angioplasty (PTCA): Report from the national heart, lung, and blood institute PTCA registry," *Am. J. Cardiol.*, vol. 53, pp. 27C–31C, 1984.
[2] D. A. Clark, *Coronary Angioplasty.* New York: Wiley-Liss, 1991.
[3] M. J. Cowley *et al.*, "Acute coronary events associated with percutaneous transluminal coronary angioplasty," *Am. J. Cardiol.*, vol. 53, pp. 12C–16C, 1984.
[4] ——, "Emergency coronary bypass surgery after coronary angioplasty, the national heart, lung, and blood institutes' percutaneous transluminal coronary angioplasty registry experience," *Am. J. Cardiol.*, vol. 61, pp. 22C–26C, 1988.
[5] D. R. Holmes, "Restenosis after percutaneous transluminal coronary angioplasty (PTCA): A report from the PTCA registry of the national heart, lung, and blood institute," *Am. J. Cardiol.*, vol. 53, pp. 77C–81C, 1984.
[6] M. Nobuyoshi *et al.*, "Restenosis after successful percutaneous transluminal coronary angioplasty: Serial angiographic follow-up of 229 patients," *J. Am. Coll. Cardiol.*, 1988.
[7] J. F. Hiehle *et al.*, "Nd-YAG laser fusion of human atheromatous plaque-arterial wall separations *in vitro*," *Am. J. Cardiol.*, vol. 56, pp. 953–957, 1985.
[8] J. R. Spears, "PTCA restenosis: Potential prevention with laser balloon angioplasty (LBA)," *Am. J. Cardiol.*, vol. 60, pp. 61B–64B, 1987.
[9] C. M. Rappaport and F. R. Morgenthaler, "Localized hyperthermia with electromagnetic arrays and the leaky wave troughguide applicator," *IEEE Trans. Microwave Theory Tech.s,* vol. 34, pp. 636–643, 1986.
[10] A. W. Guy, "History of biological effects and medical applications of microwave energy," *IEEE Trans. Microwave Theory Tech.,* vol. 32, pp. 1182–1200, 1984.
[11] C. A. Balanis, *Advanced Engineering Electromagnetics.* New York: Wiley, 1989.
[12] J. A. Stratton, *Electromagnetic Theory.* New York: McGraw-Hill, 1941.
[13] A. Rosen and P. Walinsky, "Percutaneous transluminal microwave catheter angioplasty," U.S. Patent 4 643 186, Feb. 17, 1987.
[14] A. Rosen, P. Wallinski, D. Smith, Y. Shi, Z. Kosman, A. Martinez-Hernandez, H. Rosen, F. Sterzer, D. Mawhinney, A. Presser, J. Chou, P. Goth, and G. Lowery, "Percutaneous transluminal microwave balloon angioplasty," *IEEE Trans. Microwave Theory Tech.,* vol. 38, pp. 90–93, 1990.
[15] M. Mirotznik, N. Engheta, and K. Foster, "Heating characteristics of thin helical antennas with conducting cores in a lossy medium I: Noninsulated antennas," *IEEE Trans. Microwave Theory Tech.,* vol. 41, pp. 1878–1886, 1993.
[16] A. Rosen and F. Sterzer, "Applications of microwave heating in medicine," in *1994 IEEE MTT Symp. Dig.,* 1994, pp. 1615–1618.
[17] S. Labonté, H. O. Ali, and L. Roy, "Monopoles for microwave catheter ablation of heart tissue," in *1995 IEEE MTT Symp. Dig.,* 1995, pp. 303–306.
[18] C. Rappaport, "Balloon angioplasty device," U.S. Patent 5 470 352, Nov. 28, 1995.
[19] C. Rappaport and P. Liu, "A helical microwave antenna for welding plaque during balloon angioplasty," in *1992 IEEE EMBS Symp. Dig.,* Oct. 1992, pp. 260–261.
[20] R. E. Collin, *Field Theory of Guided Waves.* New York: McGraw-Hill, 1960.
[21] B. Mukherji and H. Slouiter, "A stable perfluoro chemical blood substitute," *Transfusion,* vol. 31, pp. 324–326, 1991.
[22] M. Abramowitz and I. A. Stegun, *Handbook of Mathematical Functions with Formulas, Graphics, and Mathematical Tables.* U.S.: National Bureau of Standards, 1972.
[23] *Boston Scientific, Inc. Product Literature.* Watertown, MA: 1991.
[24] P. Liu and C. Rappaport, "A helical microwave antenna for assisting balloon angioplasty," *PIERS,* p. 545, July 1995.
[25] A. W. Guy, "Analysis of electromagnetic fields induced in biological tissues by thermographic studies on equivalent phantom models," *IEEE Trans. Microwave Theory Tech.,* vol. 19, pp. 205–214, 1971.
[26] P. Liu, C. Rappaport, Y. Wei, and S. Sridhar, "Simulated biological materials at microwave frequencies for the study of electromagnetic hyperthermia," in *1992 IEEE EMBS Symp. Dig.,* Oct. 1992.

Ping Liu received the B.S. and a M.S. degrees in electrical engineering from Shanghai Jiao Tong University, Shanghai, China, in 1985 and 1988, respectively. She received the Ph.D. degree in electrical engineering from Northeastern University, Boston, MA in 1995.

She has worked as a Research Assistant at Northeastern University from 1991 until 1995. She is currently Software Engineer at Univision Technologies, Inc., MA.

Carey M. Rappaport for a photograph and biography, see this issue, p. 1777.